Swirling Impeller Flow

H. Krain
Research Engineer,
DFVLR, Institut für Antriebstechnik,
Cologne, Federal Republic of Germany

The results of extensive laser measurements carried out in the blade passages of a newly designed backswept impeller are presented and discussed. Noticeable distortions of the throughflow patterns and a distinct swirling flow character were found inside the rotor. The measurement results and a simple theoretical approach suggest that the distorted throughflow patterns and the secondary flows are caused by a vortex flow. Although the relative flow has been significantly decelerated a comparatively smooth velocity profile has been identified at the rotor discharge that differed widely from the well-known jet/wake-type flow pattern.

Introduction

The actual discharge flow pattern of centrifugal compressor impellers is known to differ frequently from the ideal pattern predicted by potential theoretical calculation methods [1–3]. Usually, the actual flow pattern is assumed to be of the jet/wake type, generated by Coriolis, curvature, boundary layer, and tip clearance effects that separate the high and low-velocity fluid, resulting in an accumulation of low-kinetic-energy fluid in the shroud/suction side area and a collection of high-kinetic-energy fluid in the hub/pressure side area [1]. The philosophy indicated was confirmed by the laser measurements published by Eckardt in 1976 [2] and since that time this has been a widely accepted idea of the jet/wake development inside centrifugal impellers. Many scientists and design groups have tried to model the Eckardt flow pattern [4, 5]. Meanwhile, there have been some indications in the literature suggesting that the discharge flow pattern of centrifugal impellers can look quite different [3, 6]. Recently, Hamkins et al. [6] published their laser data taken in an unshrouded pump impeller showing a jet/wake development which is almost contrary to the flow character of the Eckardt impeller; i.e., in the pump impeller investigated the wake development was found close to the pressure side, whereas, in the Eckardt impeller, the wake was developing along the suction side. Obviously centrifugal impeller aerodynamics is rather complex and not yet completely understood.

However, the laser data to be presented in this paper will contribute to a further clarification of centrifugal impeller aerodynamics. Extensive laser measurements carried out within a newly designed impeller [7] and detailed studies of the vortex structure inside of the impeller gave evidence of basic flow phenomena that had not been detected in the past. The results obtained gave rise to a new view of the old jet/wake idea showing that the jet and the wake are part of a single flow phenomenon.

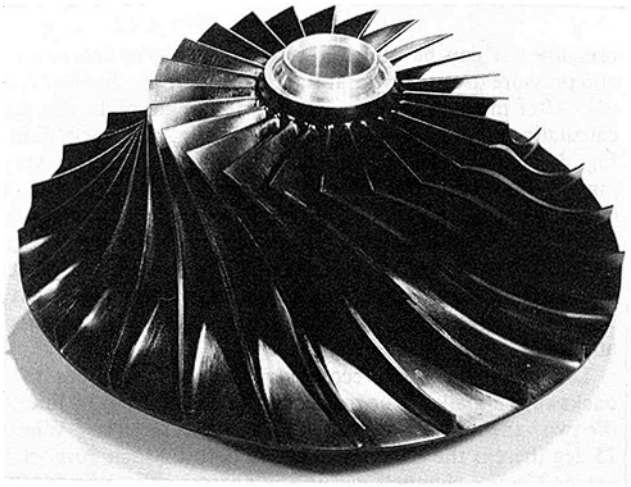

Fig. 1 30-deg backswept test impeller ($z_r = 24$)

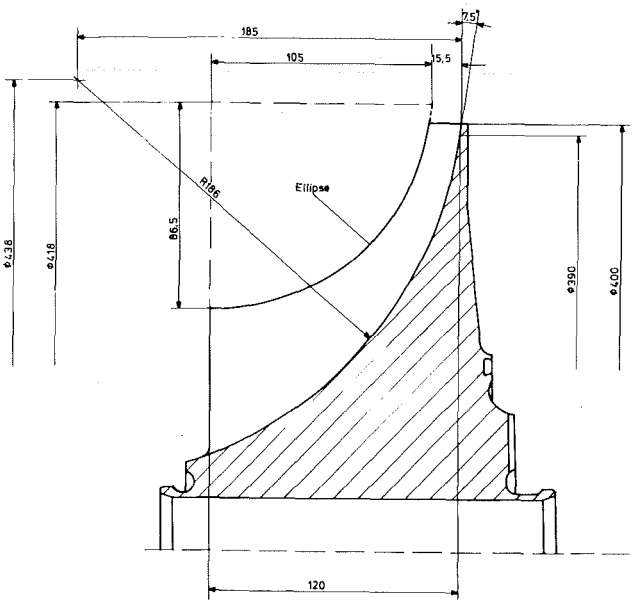

Fig. 2 Meridional cross section of the test impeller

Contributed by the Gas Turbine Division of The American Society of Mechanical Engineers and presented at the 32nd International Gas Turbine Conference and Exhibit, Anaheim, California, May 31–June 4, 1987. Manuscript received at ASME Headquarters February 3, 1987. Paper No. 87-GT-19.

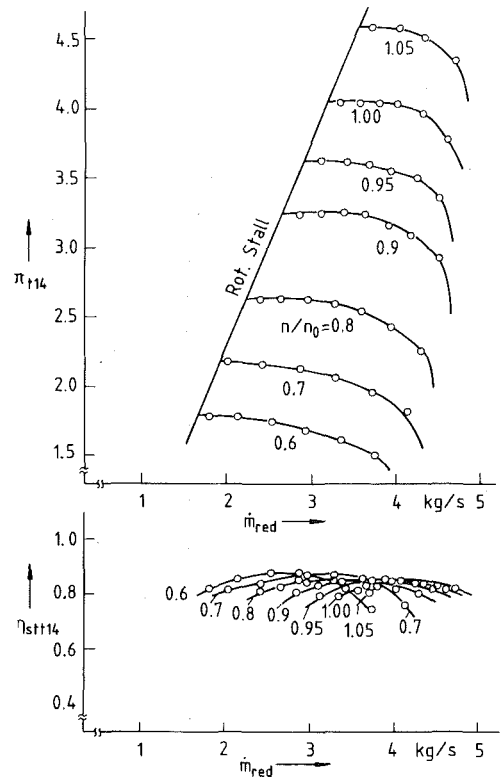

Fig. 3 Performance map of the centrifugal compressor stage composed of the test impeller and a vaneless constant area diffuser

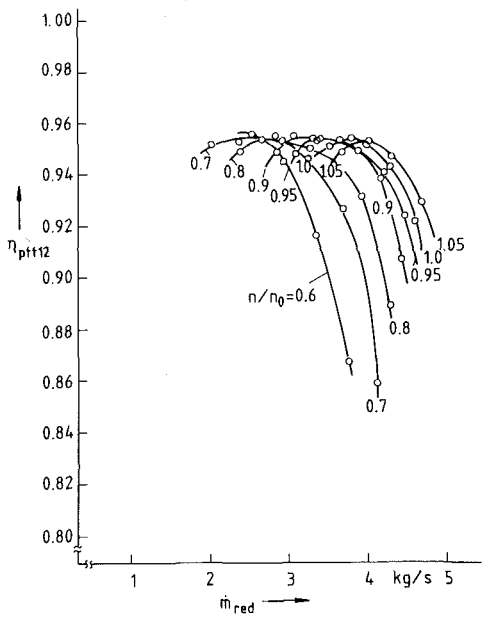

Fig. 4 Total/total polytropic impeller efficiency

Test Impeller

The impeller used for the flow analysis was a 30-deg backswept impeller which was designed by a CAD method described in detail in [7]. Figure 1 shows a photo of the impeller, and the meridional impeller cross section is submitted in Fig. 2. For the initial performance and laser measurements the impeller was coupled with a vaneless constant area diffuser that ensured a relatively wide flow range. For performance measurements total pressures and total temperatures have been measured at the inlet and exit of the compressor stage. Additionally, the static pressure development has been measured from rotor inlet to diffuser exit. The performance characteristics of the compressor stage are shown in Fig. 3. Maximum achieved total stage pressure ratio was about 4.5:1 and the maximum achieved total/total isentropic stage efficiency was 84 percent. The impeller efficiency has been deduced from total temperature, mass flow, and static pressure measurements taken by 24 tappings that were circumferentially distributed at the impeller discharge. The impeller efficiency has been derived by using the equations of energy and continuity and by assuming a zero blockage at the impeller exit.

Figure 4 shows the corresponding total/total polytropic impeller efficiency. For this first build ($N_s = 80$) that used the new design approach [7], a maximum impeller efficiency of 95 percent was achieved.

Velocity Measurements

The internal flow field of the new impeller was analyzed with the L2F technique available at DFVLR. The measurement system gives information about the magnitude and direction of the mean absolute flow vector and its turbulent components. The relative flow vector can be deduced from the velocity triangle. The error of mean absolute velocity

Nomenclature

c = absolute velocity
c_m/u_2 = meridional velocity/tip speed
c_ϕ = circumferential vortex velocity
c_{ϕ_L} = component of c_ϕ measured by L2F
HU = hub
$\dot{m}$ = mass flow rate
N_s = specific speed
n/n_0 = shaft speed/design speed
PS = pressure side
p = static pressure
r = radius
r_{max} = maximum radius of vortex
r_0 = radius of solid-body vortex
SH = shroud
SS = suction side
u = circumferential velocity
w_b = velocity parallel to the blade
w_L = velocity measured by L2F
w_r = radial velocity component
w_z = axial velocity component
w_ϕ = circumferential vortex velocity (Fig. 20)
x, y = Cartesian coordinates
x/s_m = dimensionless shroud length
y/t = dimensionless blade pitch
z/b = dimensionless channel depth
z_r = rotor blade number
β_b = blade angle
β_L = flow angle measured by L2F (Fig. 13)
$\Delta\beta_R$ = flow angle difference (Fig. 22)
δ = swirl parameter (Fig. 22)
η_{stt} = total/total isentropic efficiency
η_{ptt} = total/total polytropic efficiency
ν = kinematic viscosity
π_t = total pressure ratio
ϕ = circumferential coordinate
ω = angular velocity of the solid-body vortex

Subscripts

0 = ambient condition
1 = impeller inlet
2 = impeller exit
3 = vaned diffuser inlet
4 = diffuser exit
red = corrected

Table 1 Positions of L2F measurement planes (Fig. 5)

Measurement plane	Locations x/s_m
I	0
II	0.2
III	0.4
IV	0.6
V	0.8
VI	1.004

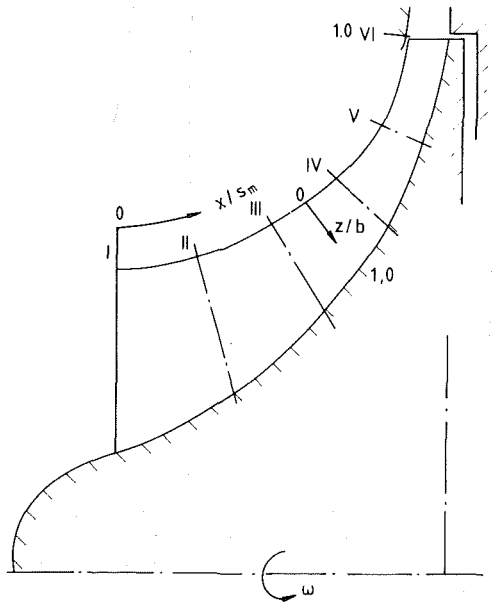

Fig. 5 Arrangement of the L2F measurement planes

measurements is usually less than ±1 percent and the uncertainty of absolute flow angle measurements generally is less than ±1 deg. Therefore, for the backswept impeller, the uncertainty of the relative flow angles is less than ±0.5 deg, which can be derived from the velocity triangle. Further details about that measurement technique and its applicability to turbomachinery flows even under complex flow conditions are given in [8]. Measurements in the backswept impeller were performed at 70, 90, and 100 percent shaft speed. For each speed three mass flow rates were selected, located close to stall, at peak efficiency and close to surge (Fig. 3). The results presented in this paper were taken at the impeller design point ($n/n_0 = 1.0$, $\dot{m}_{red} = 4.0$ kg/s). Six measurement planes have been selected in the rotor area to analyze the internal flow field (Fig. 5). The measurement planes are perpendicular to the shroud casing throughout and their positions within the rotor are listed in Table 1.

The flow conditions at the impeller exit are generally believed to influence both flow range and efficiency of centrifugal compressor stages. Usually, the flow character present at the impeller exit already gives some insight into the quality of the overall impeller flow and into the diffuser inlet flow conditions. Therefore, laser measurements were started at plane VI, which coincides with the impeller exit (Table 1).

The result of these measurements is given in Fig. 6, which shows a comparison of three velocity profiles measured at the exits of three different impellers. The pattern at the top belongs to the radially ending Eckardt impeller [2], the pattern in the middle has been found close to the exit ($x/s_m = 0.89$) of a radially ending splitter blade impeller [3], and the flow pattern at the bottom has been analyzed at the exit of the new impeller. For each impeller the measured meridional velocity referred to the rotor tip speed c_m/u_2 is plotted versus flow area. It should be noted that the specific speeds of the radially ending impellers ($N_s = 115$) differed from that of the

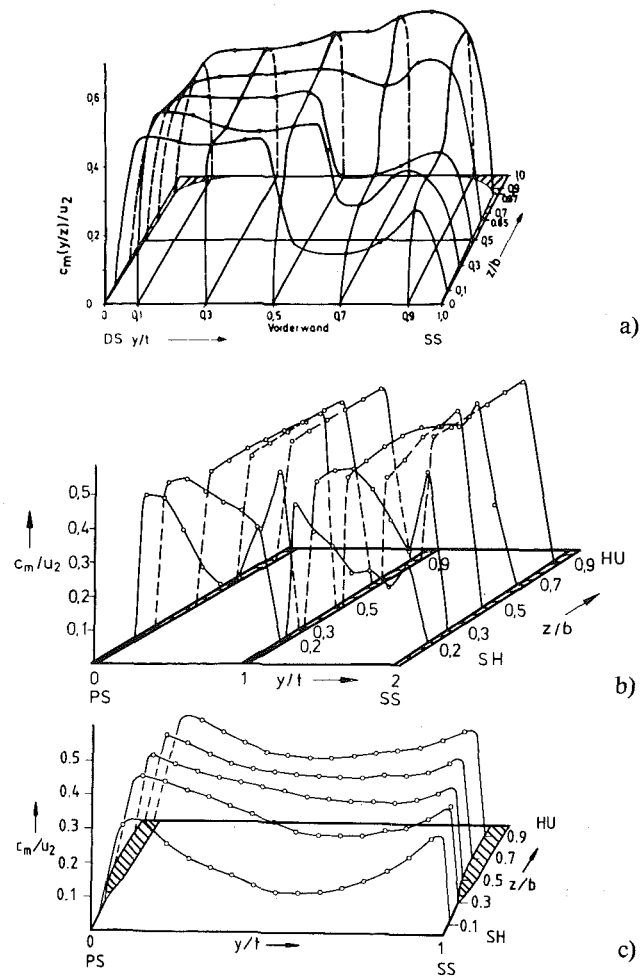

Fig. 6 Comparison of velocity profiles: (a) radially ending Eckardt impeller, 20 long blades [2]; (b) radially ending splitter-blade impeller, 14 + 14 blades [3]; (c) new backswept impeller (Figs. 1, 2)

backswept impeller ($N_s \approx 80$). Additionally, measurements at the exits of the radially ending impellers were carried out at pressure ratios of about 2:1 whereas the pressure ratio of the stage equipped with the new backswept impeller was 4:1 (Fig. 3).

Figure 6 clearly shows that a very smooth velocity profile, primarily in the pitchwise direction, is present at the discharge of the new impeller. A highly disturbed velocity profile resembling the classical jet/wake pattern is not seen at the exit of the new impeller. Above all, a smooth discharge flow was obtained, although the relative flow within the new impeller has been much more decelerated than the flow within the radially ending impellers, which agrees fairly well with the high impeller efficiencies shown in Fig. 4. An accumulation of flow with low kinetic energy is only observed very close to the shroud ($z/b = 0.1$) and outside of the impeller (Fig. 5). Tip clearance and mixing effects were at first believed to generate this flow character.

In summary, the design goals of this first build were met and we speculated whether it would make any sense to continue the laser measurements since it was believed that an impeller having such a smooth discharge flow pattern will also have a regular pattern throughout the rotor. However, measurements were continued proceeding from rotor inlet to rotor exit. The results obtained were rather surprising.

Figures 7 and 8 show the measured velocity profiles at planes I and II. As expected, the patterns are very regular and

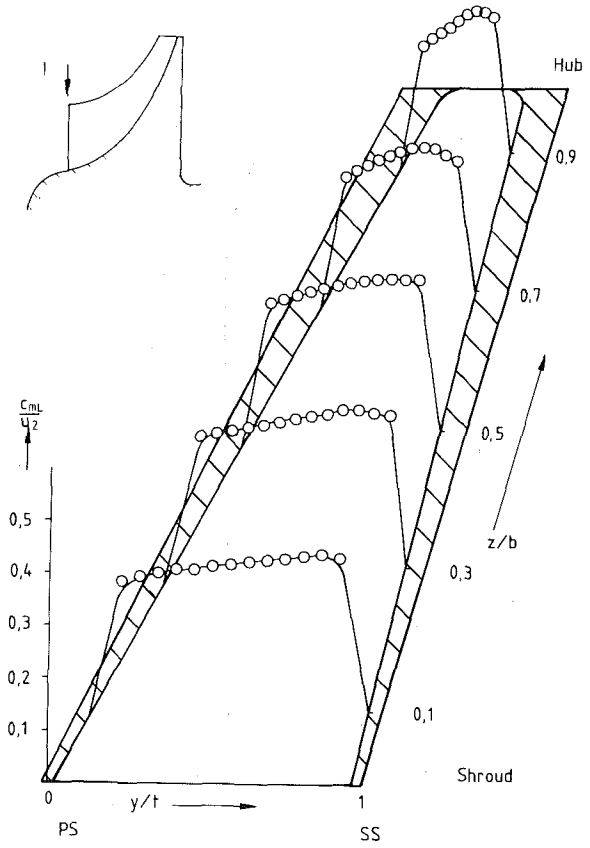

Fig. 7

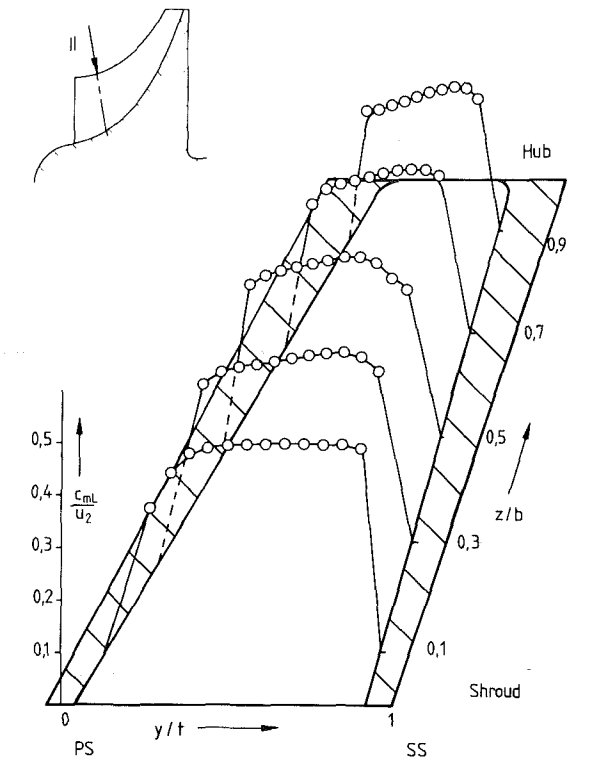

Fig. 8

the meridional velocity exhibits a positive gradient from the pressure to the suction side. Surprisingly, an unexpected irregular distribution of the meridional velocity profile was determined close to the shroud of plane III ($z/b=0.1$, Fig. 9) and the point of minimum velocity at this measurement position is located in the pressure side area rather than in the suction side area ($y/t=0.3$). From plane III to plane IV the point of minimum velocity shifts toward the middle of the flow channel and the disturbed flow now has extended covering about 50 percent of the channel depth (Fig. 10). Close to the impeller exit, however, the meridional velocity profile is smoothing again (Fig. 11) and the exit flow (Fig. 12) is even more regular in the pitchwise direction.

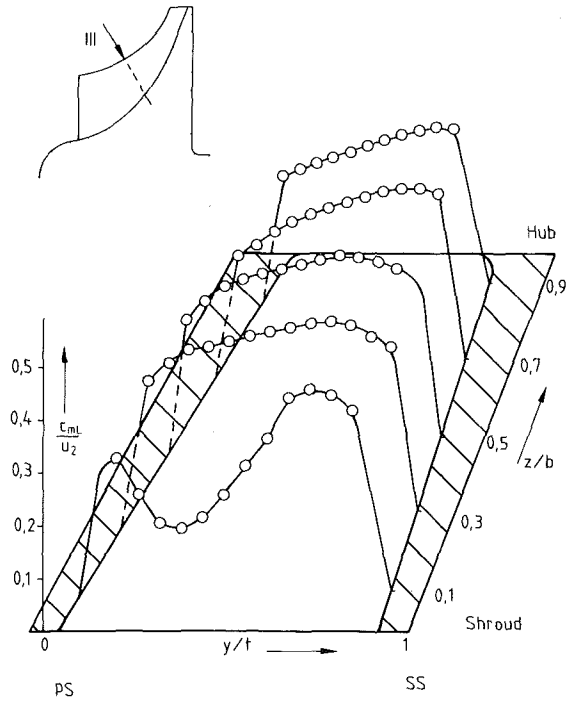

Fig. 9

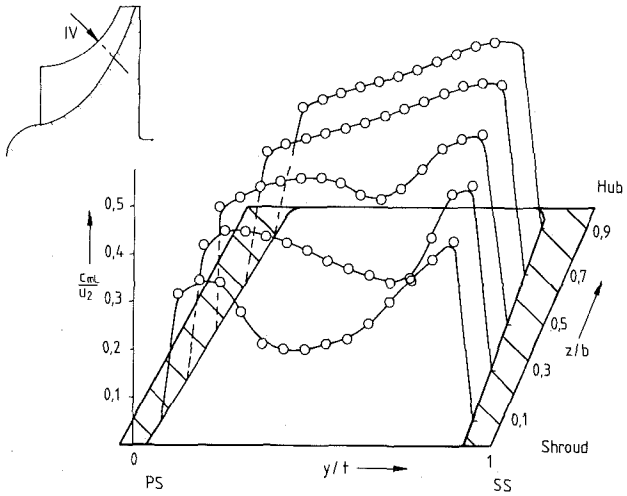

Fig. 10

In summary, the velocity patterns shown in Figs. 7–12 suggest that a wake flow is also present in this impeller. But in contrast to the original jet/wake philosophy previously pointed out and in contrast to the measurements available for radially ending impellers [2, 3], the wake now has a maximum inside the impeller and it decreases toward the impeller exit. Formerly, such a flow development has not been experienced. In order to get a better understanding of this type of impeller flow, a new data analysis procedure was applied that indeed gave more insight into the governing physical flow effects of that impeller.

Vortex Analysis by the L2F Technique

The most important information was extracted from the

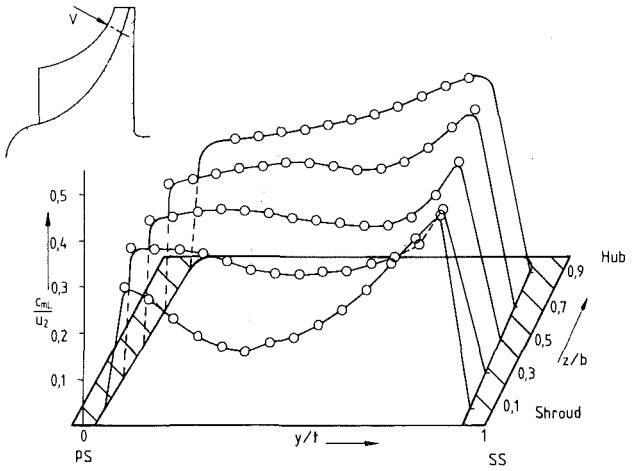

Fig. 11

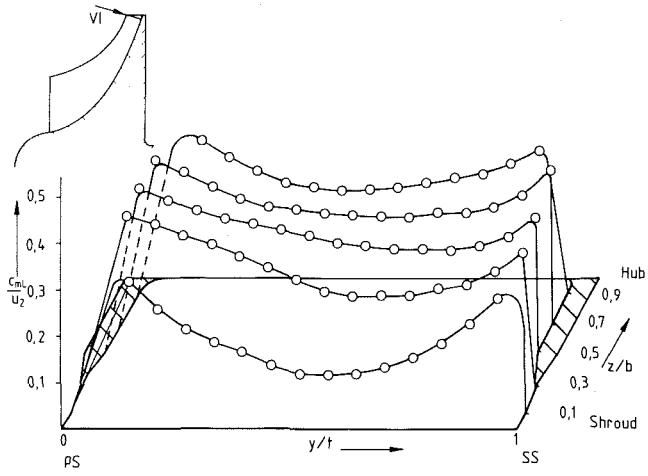

Fig. 12

Figs. 7-12 Meridional velocity profiles measured at planes I-VI ($n/n_0 = 1$, $\dot{m}_{red} = 4.0$ kg/s)

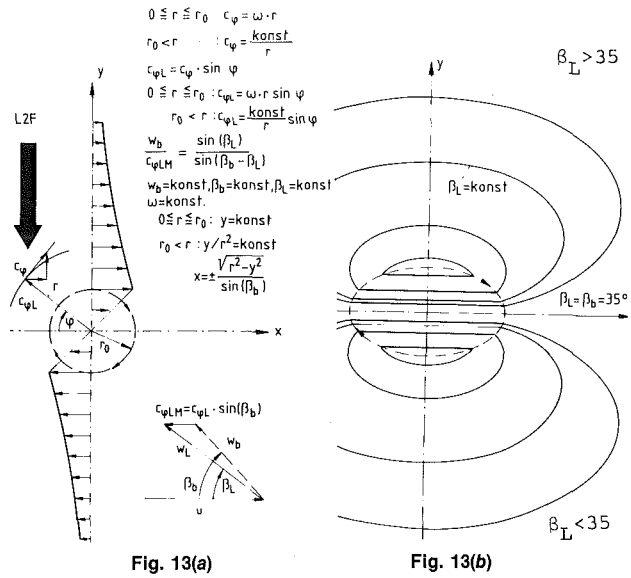

Fig. 13(*a*) Fig. 13(*b*)

Fig. 13 Measurement of vortex flow with L2F-technique

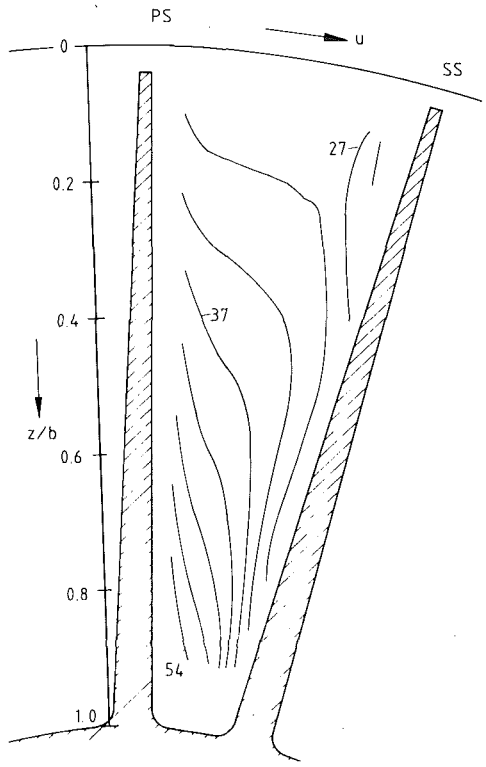

Fig. 14

lines of constant flow angle (isoclines) plotted for the six measurement planes (Fig. 5). The shape of these isoclines gives information about the vortex flow within the impeller area. The basic equations for the isoclines of a real vortex, composed of a solid-body vortex and a potential vortex, are submitted in Fig. 13(*a*) and the result of the analysis for a throughflow inclined against the drawing plane ($\beta_b = 35$ deg) is shown in Fig. 13(*b*). Lines of constant flow angle are parallel in the solid-body vortex area ($0 \le r \le r_0$) whereas these lines are of elliptic type in the potential vortex area ($r > r_0$). The vortex center is always located in the middle of the parallel isoclines. The approach presented was originally applied by Binder [10] and has been used to identify a vortex flow within the impeller area. A real vortex, composed of a solid-body vortex and a potential vortex, was assumed to be present when isoclines similar to those shown in Fig. 13(*b*) were analyzed.

Flow Angle Analysis

Figures 14-19 show the results of the detailed flow angle analysis carried out for all measurement planes. At plane I (Fig. 14) the relative flow angle varies from 54 to 28 deg from hub to shroud, which is in agreement with the design specifications. At plane II (Fig. 15) the isoclines are primarily horizontal. Closed lines of constant flow angle, which may be interpreted as counterrotating corner vortices, are found in the shroud area. At plane III (Fig. 16), where the first distortion of the throughflow was analyzed (Fig. 9), the isoclines for the first time exhibit a shape similar to that shown in Fig. 13. At plane IV (Fig. 17) the isocline pattern represents all features illustrated in Fig. 13. At this measurement position two counterrotating channel vortices are clearly identified. The centers of these vortices are roughly indicated. Additionally, parallel isoclines and a strong gradient in flow angle are present close to the shroud. However, a clearly developed vortex like that found in the middle of the flow channel is not resolved in this area. Obviously, a swirling flow covering the entire flow channel is present at this measurement plane. A similar flow character is seen at plane V (Fig. 18). The centers

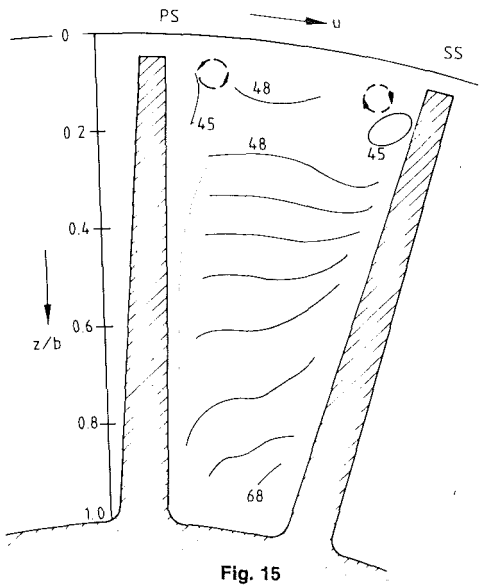

Fig. 15

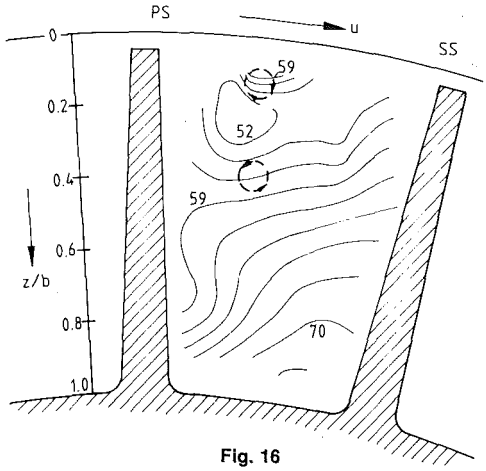

Fig. 16

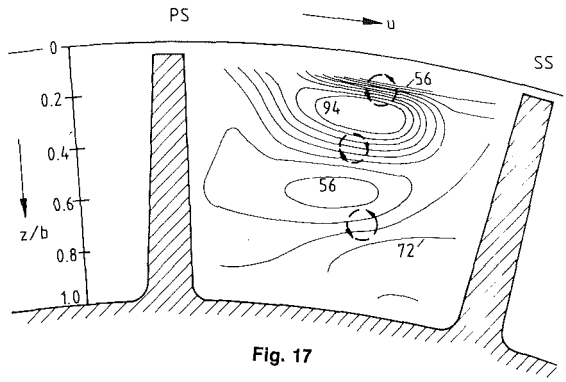

Fig. 17

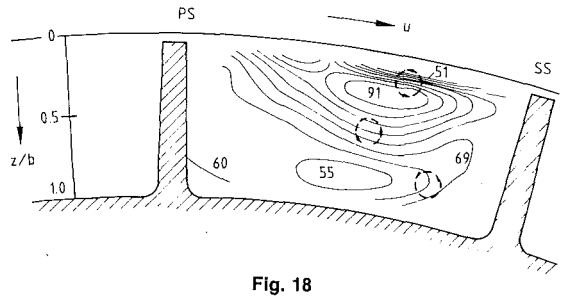

Fig. 18

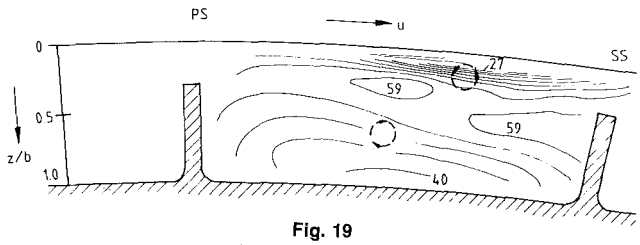

Fig. 19

Fig. 14-19 Isocline patterns (β_L = const) measured at planes I-VI ($n/n_0 = 1$, $m_{red} = 4.0$ kg/s)

of the channel vortices have now shifted toward the middle of the flow channel and toward the hub/suction side. The vortex flow is again dominating the entire flow channel. A different pattern is present at the rotor exit (plane VI, Fig. 19). Here, only one channel vortex center is seen; the second has disappeared. But again the strong gradient in flow angle and the parallel isoclines are present close to the shroud. Obviously, the swirling flow present in any unshrouded impeller has a dominating influence on the overall flow development of the new backswept impeller. The isocline plots (Figs. 14–19) suggest that the swirling impeller flow, covering at least the entire flow channel, is initiated by the relative motion between the moving rotor and the stationary casing. Thus, this flow character seems to have its origin in the shroud area.

Vortex Flow and Throughflow

A comparison between Figs. 7–12 and Figs. 14–19 reveals that the distortions in the throughflow patterns have always been identified in those areas where the vortex flow is active. So, the question arises whether these flow phenomena belong together. A first answer of this question is obtained by a simple approach to the Navier–Stokes equations. A vortex flow with a zero radial velocity component ($w_r = 0$) and a throughflow component varying only in the radial direction ($w_z = w_z(r)$) was assumed. The remaining terms of the Navier–Stokes equations for these assumptions are submitted in Fig. 20. The throughflow velocity distribution $w_z = w_z(r)$ can be easily derived from the last equation. Figure 20 il-

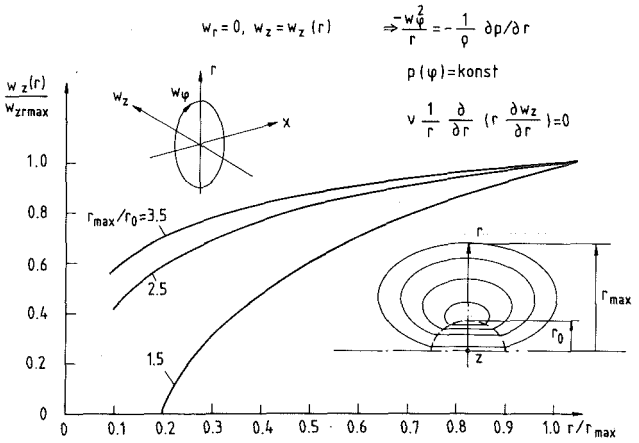

Fig. 20 Axial velocity distribution in a vortex

lustrates the result of this approach for three vortices. Obviously, the throughflow velocity is decreasing toward the vortex center and the declining rate is dependent on the vortex structure. This result qualitatively agrees with the measurement results found for the new backswept impeller and suggests that the distortions found in the throughflow patterns of the new impeller are due to the swirling impeller flow.

These effects are well known. A theoretical result for a turbulent compressible pipe flow with prescribed inlet swirl, calculated by Neuberger [9], is shown in Fig. 21. This figure il-

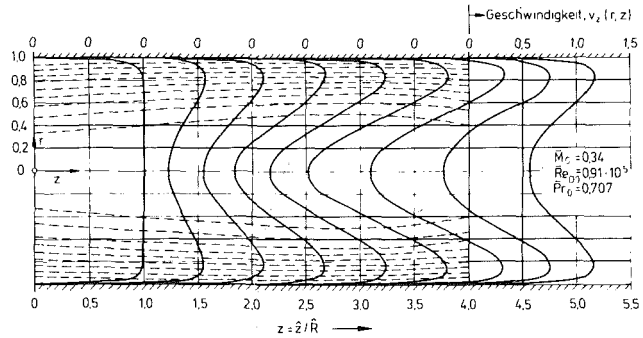

Fig. 21 Axial velocity profile development predicted for a pipe flow with prescribed inlet swirl [9]

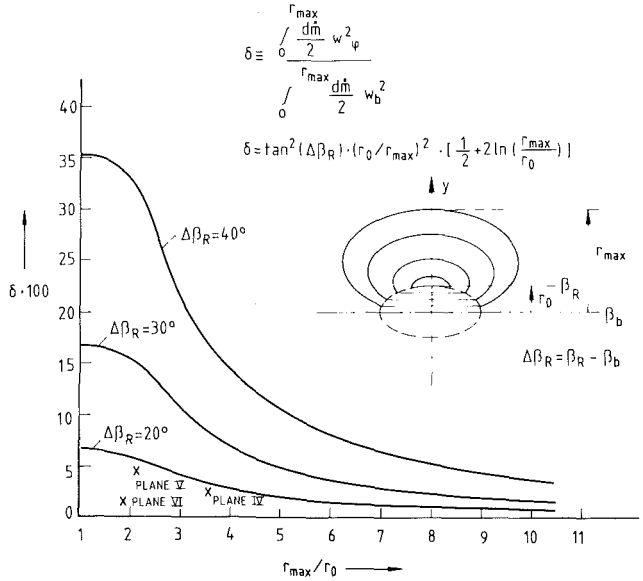

Fig. 22 Swirl parameter calculated for different vortex types; values calculated for the impeller flow are indicated by crosses

lustrates the axial velocity profile development for an inlet swirl chosen in such a way that backflow is avoided ($\hat{Z}/\hat{R}=2.5$). Obviously, the smooth axial velocity profile present at the inlet at first is distorted and is smoothed again toward the exit. A comparison with the impeller flow reveals surprising similarities. Within the new impeller the distortions in the throughflow patterns are also smoothed toward the exit (Figs. 7–12). However, compared to the pipe flow the intensity of the swirling flow within the impeller seems to be low since the distortions of the throughflow patterns are moderate and the throughflow is obviously far from backflow. Very often the swirl parameter δ defined in Fig. 22 is used for a quantitative assessment of the swirling flow intensity. With the definition of Fig. 22 the swirl parameter has been calculated for different vortices. For each calculation a real vortex, composed of a solid-body vortex and a potential vortex, has been assumed. For that vortex type a simple relation has been derived by which the swirl parameter can be calculated. The relation of Fig. 22 indicates that the amount of the swirl parameter primarily depends on the vortex shape (r_{max}/r_0) and on the flow angle difference $\Delta\beta_R$. Obviously, the swirl parameter decreases when the potential vortex part is increasing and it also strongly decreases with decreasing flow angle difference $\Delta\beta_R$.

The relation of Fig. 22 has been used to calculate a swirl parameter for the main channel vortex of the backswept impeller. The values necessary for this assessment have been taken from Figs. 17, 18, and 19. The approach already indicates that the results obtained (Fig. 22) are only a rough estimate. The swirl parameters calculated by this procedure for measurement planes IV, V, and VI are indicated by crosses in Fig. 22. Although the swirling flow seems to have a significant influence on the overall flow character at these measurement planes the corresponding swirl parameters are all less than 5 percent, indicating a rather low swirl intensity.

Conclusions

The measurement results obtained for the new backswept impeller revealed a distinct vortex flow that considerably influenced the overall rotor flow character. Secondary flows and distorted throughflow patterns were caused by the swirling impeller flow inside the rotor. But toward the rotor exit the throughflow pattern was smoothed again resulting in a relatively regular discharge flow pattern that differed widely from the well-known jet/wake-type flow pattern. The swirling intensity of the main channel vortex estimated by the swirl parameter δ was found to be rather low. The swirl parameter δ derived for the backswept impeller was less than 5 percent. With regard to a general impeller design it should be noted that a vortex flow like that analyzed here will be present in any unshrouded impeller. Since the vortex flow seems to influence the throughflow pattern too, a slightly distorted impeller discharge flow seems to be inevitable unless the flow development is guided in such a way that the vortex flow fully disappears at the impeller discharge. How to reach this aim is not easy to derive from the results presented. Theoretical models capable of predicting the internal three-dimensional viscous flow of centrifugal compressor impellers could help to extract that information.

References

1 Dean, R. C., Jr., "The Fluid Dynamic Design of Advanced Centrifugal Compressors," Creare, TN-185, July 1974, p. 76.

2 Eckardt, D., "Detailed Flow Investigations Within a High-Speed Centrifugal Compressor Impeller," ASME *Journal of Fluids Engineering*, Vol. 98, 1976, pp. 390–402.

3 Krain, H., "A Study on Centrifugal Impeller and Diffuser Flow," ASME JOURNAL OF ENGINEERING FOR POWER, Vol. 103, No. 4, 1981, pp. 688–697.

4 Moore, J., and Moore, J. G., "Three-Dimensional Viscous Flow Calculation for Assessing the Thermodynamic Performance of Centrifugal Compressors: Study of the Eckardt Compressor," AGARD-CP-282, May 1980, pp. 9.1–9.19.

5 Bosman, C., "Computation of Three Dimensional Flow Through the Eckardt Compressor Impeller," AGARD-CP-282, May 1980, pp. 10.1–10.8.

6 Hamkins, C. P., and Flack, R. D., "Laser Velocimeter Measurements in Shrouded and Unshrouded Radial Flow Pump Impellers," ASME JOURNAL OF TURBOMACHINERY, Vol. 109, 1987, pp. 70–76.

7 Krain, H., "A CAD-Method for Centrifugal Compressor Impellers," ASME JOURNAL OF ENGINEERING FOR GAS TURBINES AND POWER, Vol. 106, 1984, pp. 482–488.

8 Krain, H., Schodl, R., Binder, A., and Dunker, R., "Successes in the Application of Laser Velocimetry to Turbomachinery Studies," Principal LS No. 1, Concepts ETI, Inc., 1986, pp. 5.1–5.22.

9 Neuberger, W., "Calculation of Compressible Swirling Flows in Pipes, Annuli and on Rotating Cylinders," DFVLR-FB 80–21, p. 107 (in German).

10 Binder, A., "Instationary Flow Effects in the Rotor of a Turbine," Thesis, University of Aachen, DFVLR-FB-85-66, p. 157 (in German).